Supporting Information for:

Elucidating the Decomposition Mechanism of Energetic Materials with Di-Nitro Functional Groups Using 2-Bromo-2-Nitropropane Photodissociation

Ryan S. Booth[1], Chow-Shing Lam[1], Matthew D. Brynteson[1], Lei Wang[1] and Laurie J. Butler[1]

[1] The James Franck Institute and Department of Chemistry, University of Chicago, Chicago, Illinois 60637, USA

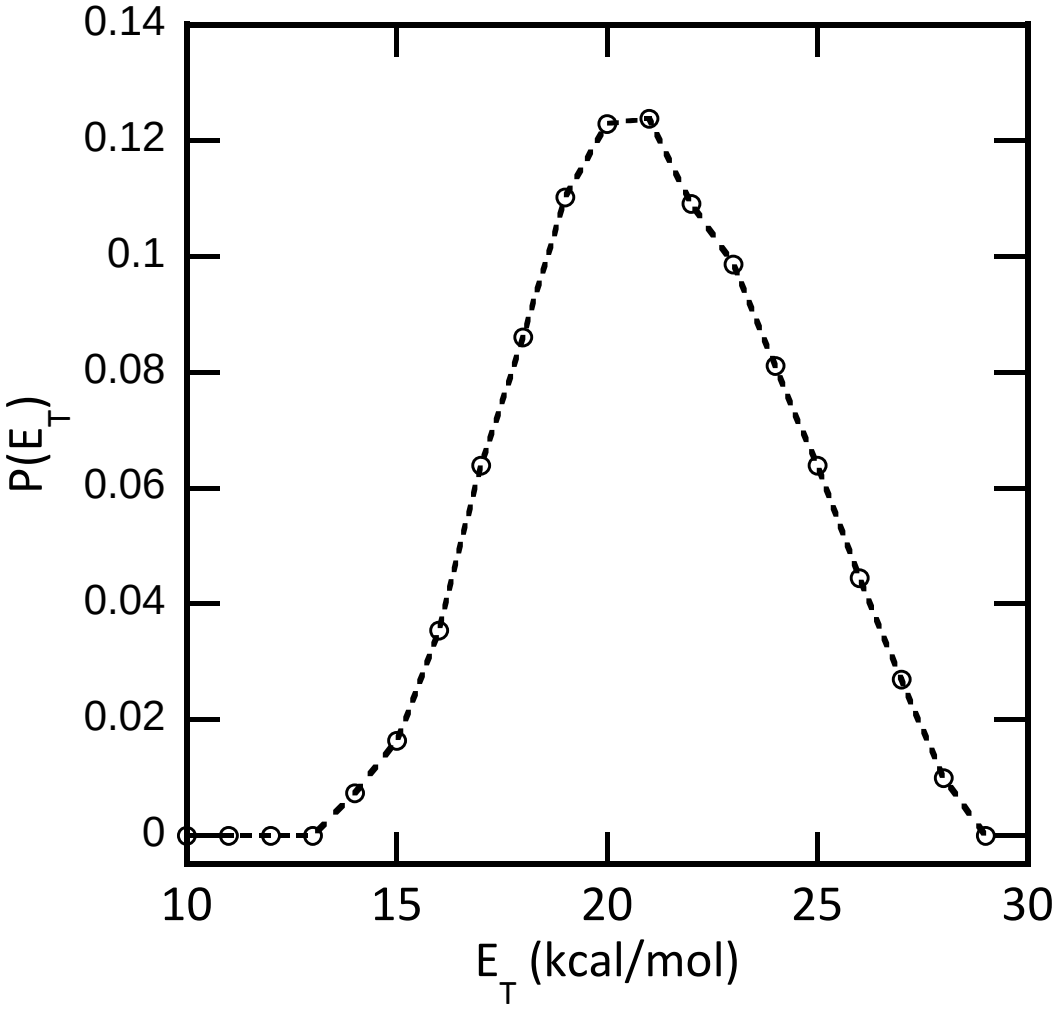

Figure S1: Product recoil kinetic energy distribution for the unimolecular dissociation of the 2-nitro-2-propyl radical to HO + $CH_3C(NO)CH_2$ (Eq. 7). It is derived from forward convolution fitting the signal at m/e=41 (10.5 eV) which does not appear at 8.87 eV ionization energy (Fig. 11, lower frame) and the signal shown in the dashed black line in the m/e=17 TOF (Fig. S2)

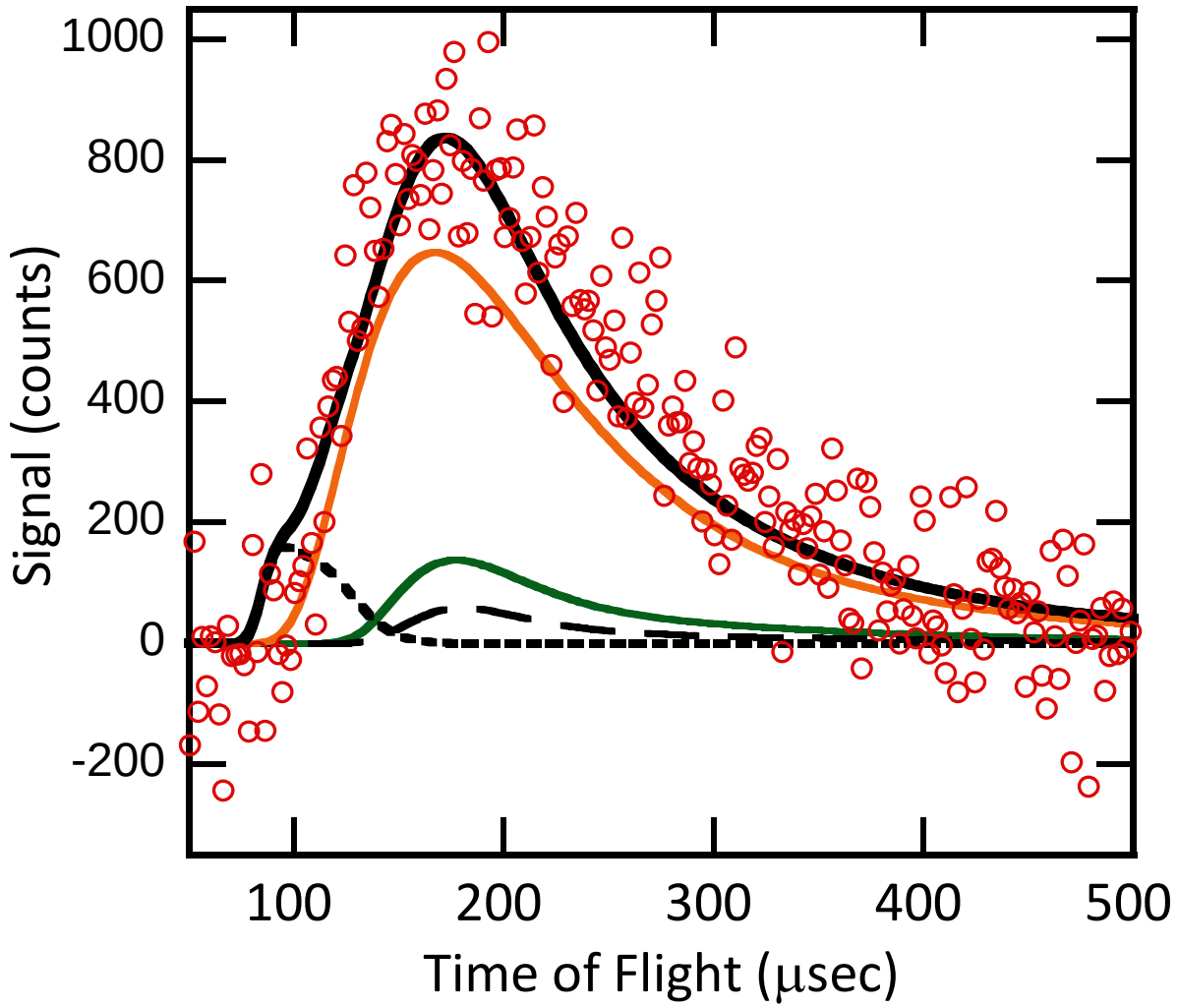

Figure S2: Time-of-flight spectrum taken at m/e=17, OH^+. Data are shown in red circles. The dashed black line fit show the contribution from OH products from the dissociation of 2-nitro-2-propyl radical to OH + $CH_3C(NO)CH_2$ (Eq. 7) using the $P(E_T)$ shown in Figure S1. The other contributions are described in the main text in Figure 15.

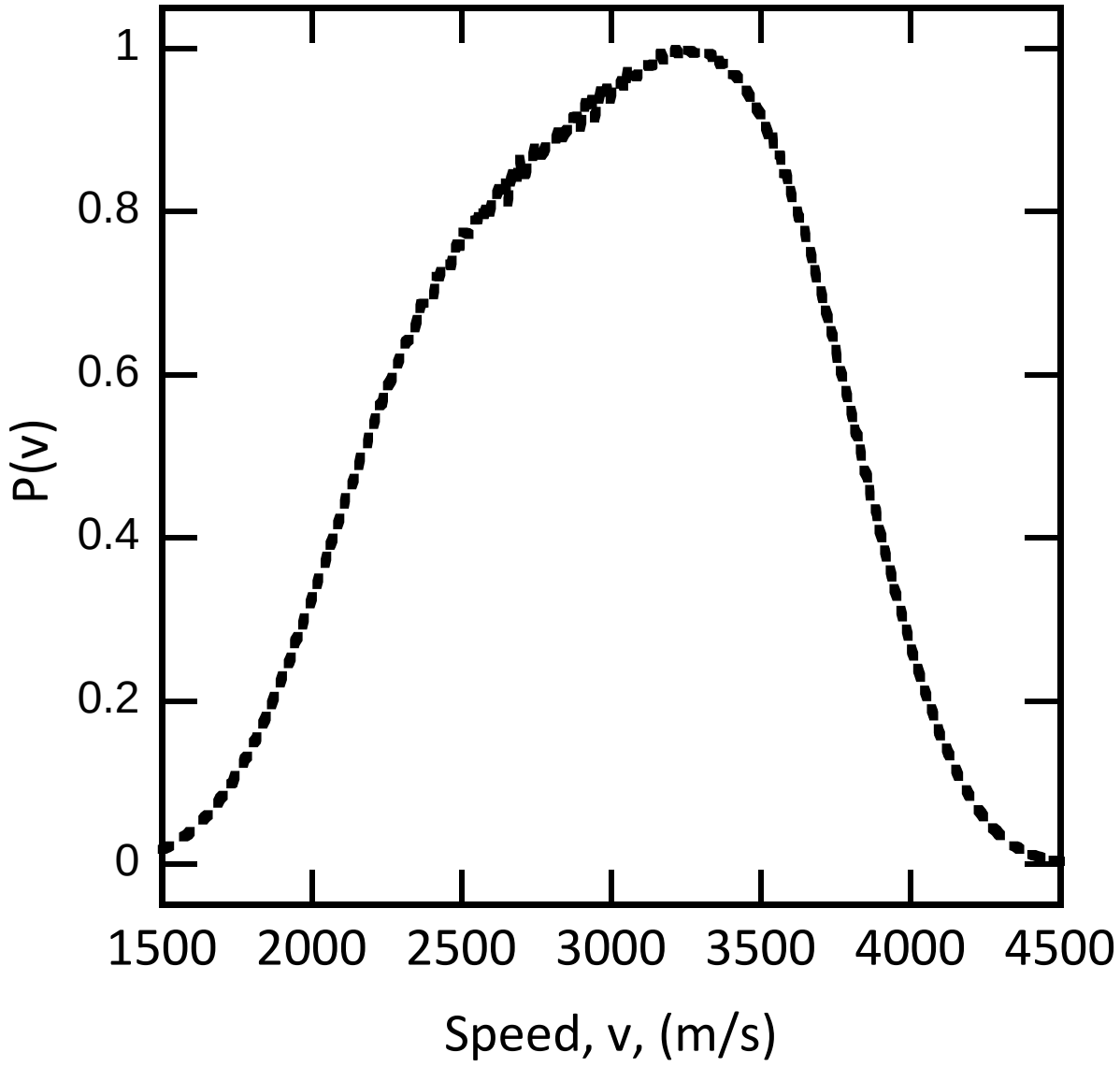

Figure S3: The predicted net speed distribution of OH fragments from the unimolecular dissociation of the 2-nitro-2-propyl radical to OH + $CH_3C(NO)CH_2$ (Eq. 7) using the $P(E_T)$ shown in Figure S1.

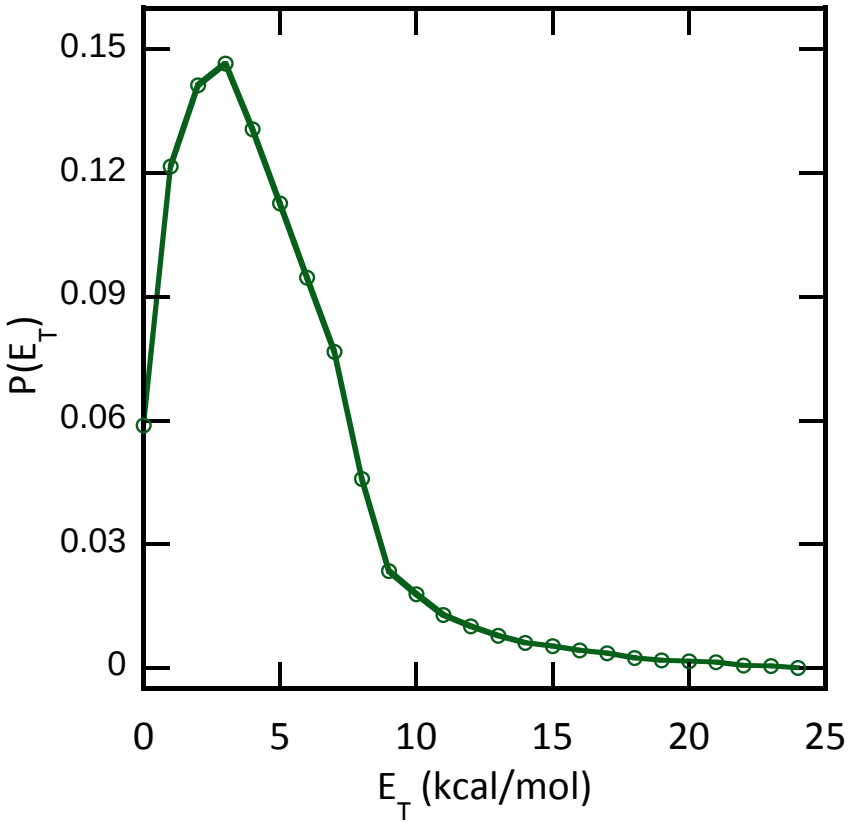

Figure S4. Product recoil kinetic energy distribution for the unimolecular dissociation of the 2-nitro-2-propyl radical to HONO + CH_3CCH_2 (Eq. 8). It is derived from forward convolution fitting the green portions of the spectra in Figures 11 and 12 (in main text) assuming an isotropic secondary angular distribution.

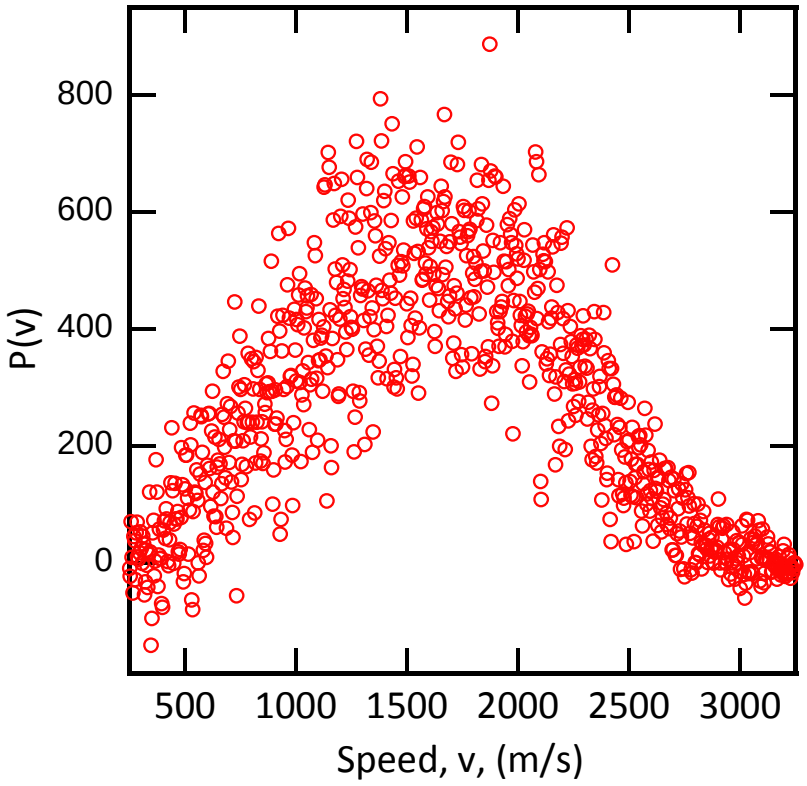

Figure S5: Speed distribution derived from the m/e=43 (CH_3CO^+) image (Fig. S6). Data are shown in red circles.

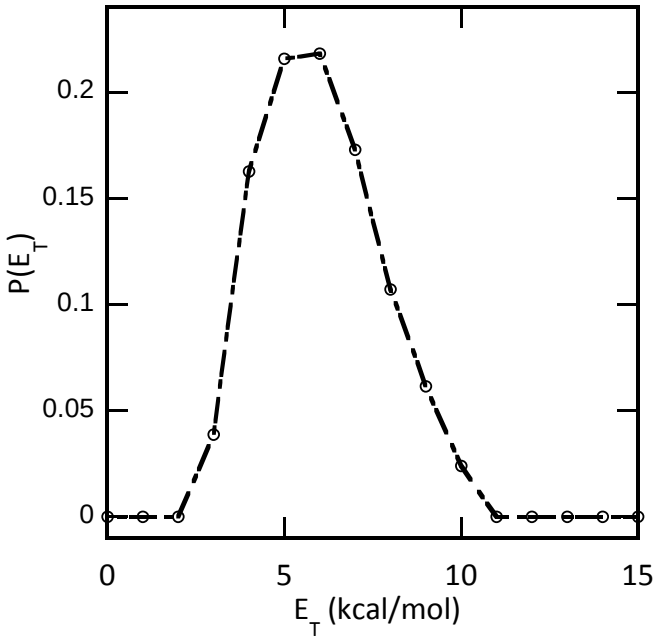

Figure S6. Product recoil kinetic energy distribution for the unimolecular dissociation of 2-nitropropene to HONO + C_3H_4 (Eq. 12). This $P(E_T, 2°)$ is created by forward convolution of the dash dot black fit in Figure 21 (in main text).

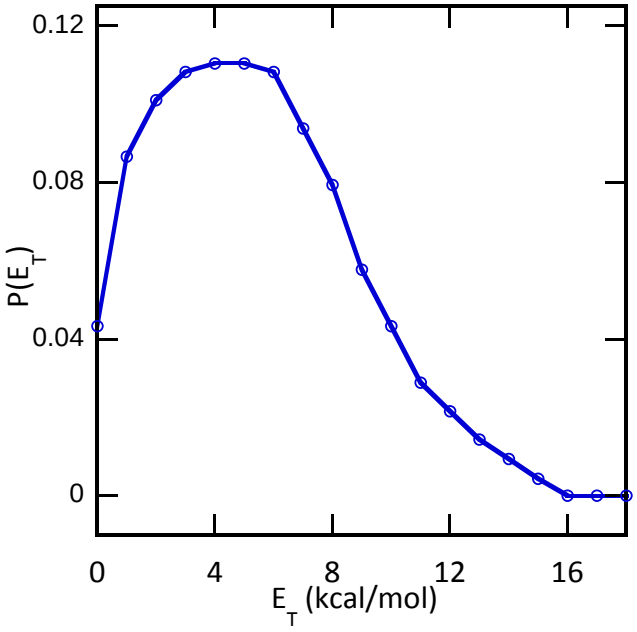

Figure S7: Product recoil kinetic energy distribution for the unimolecular dissociation of 2-nitropropene to NO + $CH_3C(O)CH_2$ (Eq. 15). This $P(E_T, 2°)$ was derived jointly with the $P(E_T, 3°)$ shown in Figure S7. The blue fit in the m/e=42 P(v) shown in Figure 22 (in main text) was used to create this $P(E_T)$ in conjunction with Figure S7.

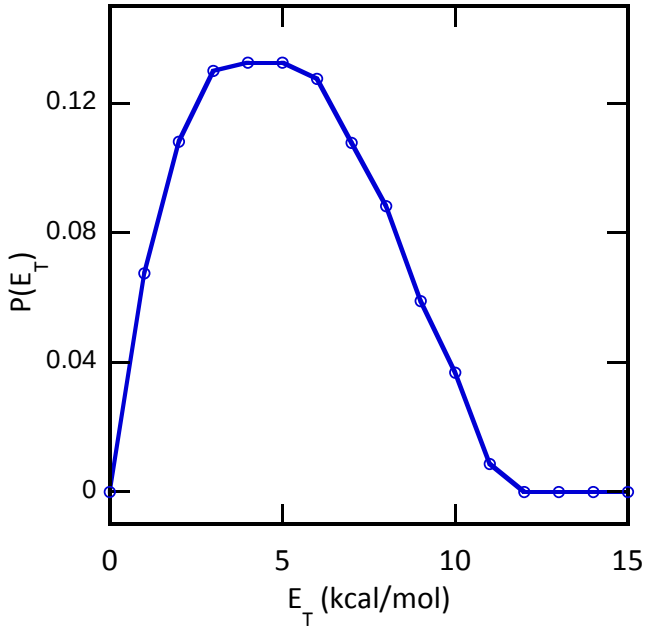

Figure S8: Product recoil kinetic energy distribution for the unimolecular dissociation of $CH_3C(O)CH_2$ to CH_3 + ketene. The blue fit in the m/e=15 (CH_3^+) TOF shown in Figure 23 (in main text) was used to create this $P(E_T, 3°)$ in conjunction with the $P(E_T, 2°)$ shown in Figure S6.

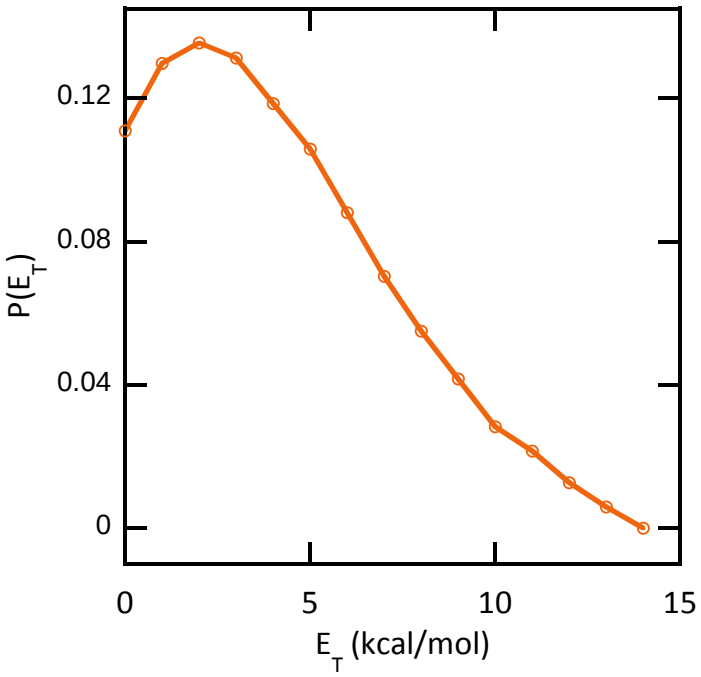

Figure S9. Product recoil kinetic energy distribution for the unimolecular dissociation of HONO to OH + NO (Eq. 16). This $P(E_T, 2°)$ is derived by forward convolution of the orange fit in the m/e=17 (OH^+) and m/e=30 (NO^+) TOF and P(v) (Figures 14, 13, 15, respectively [in main text]).

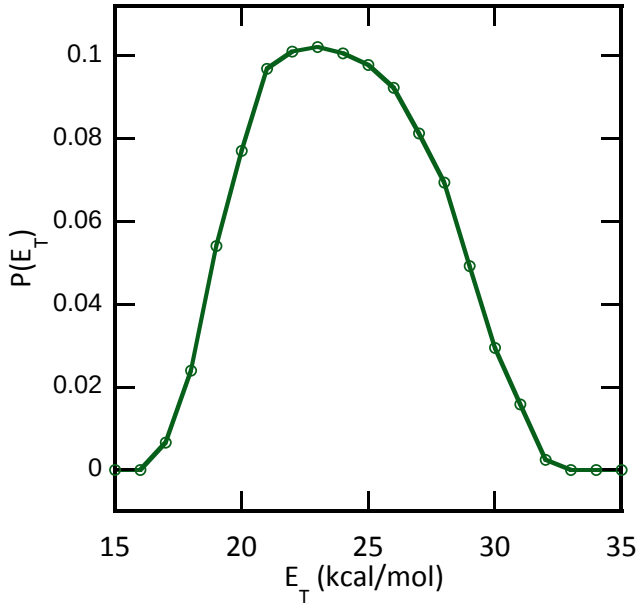

Figure S10. Product recoil kinetic energy distribution for the unimolecular dissociation of 2-bromopropene to HBr + C_3H_4 (Eq. 17). This $P(E_T, 2°)$ is derived by forward convolution of the green fit in the m/e=80 (HBr^+) TOF and m/e=40 P(v) (Figures 9 and 21, respectively [in main text].

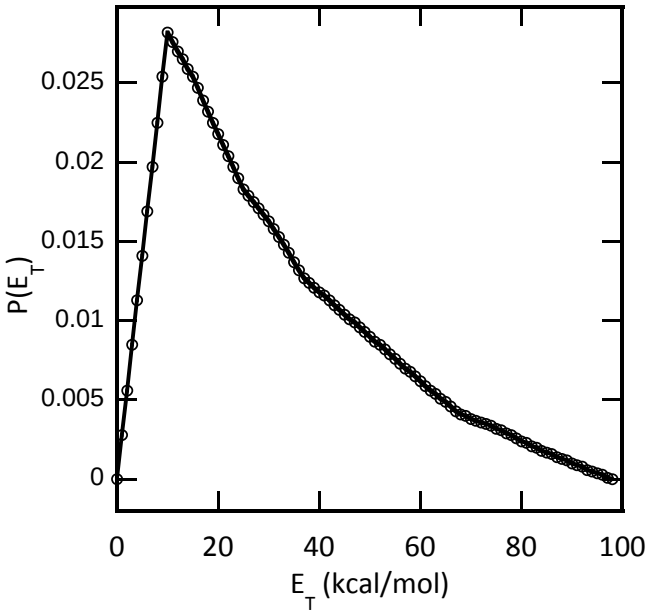

Figure S11. Product recoil kinetic energy distribution photodissociation of NO_2 fragments resulting from the primary photodissociation of 2-bromo-2-nitropropane to NO_2 + $CH_3C(Br)CH_3$ at 193 nm. This $P(E_T, h\nu, 2°)$ is reproduced from the appendix of Reference 21 (in main text). Forward convolution fitting using this $P(E_T, h\nu, 2°)$ gives the small dashed black fit in the m/e=30 TOF and P(v) shown in Figures 13 and 15, respectively (in main text).

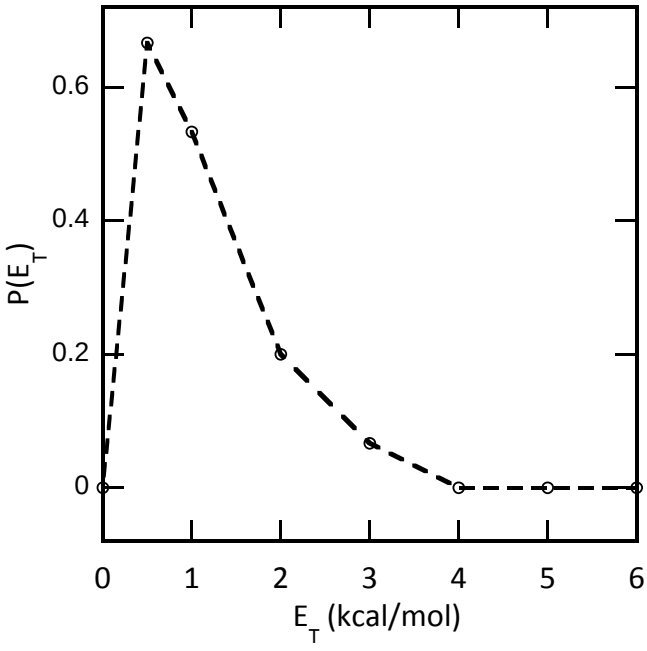

Figure S12. Product recoil kinetic energy distribution for the dissociative ionization of $CH_3C(Br)CH_3$ radicals, arising from the primary NO_2 loss, to $CH_2CHCH_3^+$ + Br. This $P(E_T, 2°)$ is derived by forward convolution of the dashed black fit in the m/e=42 ($CH_2CHCH_3^+$) P(v) shown in Figure 22 (in main text).

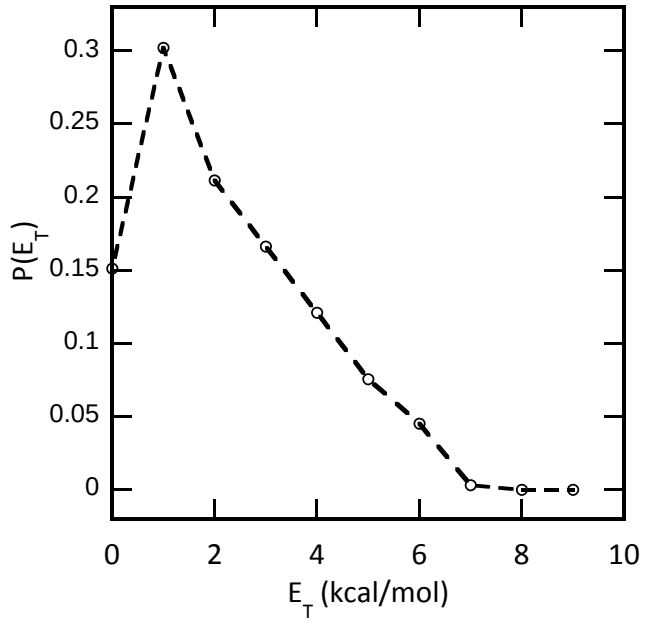

Figure S13. Product recoil kinetic energy distribution for the dissociative ionization of $CH_3C(Br)CH_3$ radicals, arising from the primary NO_2 loss, to $CH_3CCH_2^+$ + HBr. This $P(E_T, 2°)$ is derived by forward convolution of the short dashed black line fit in the m/e=41 ($CH_2CCH_3^+$) P(v) shown in Figure 11 (in main text).

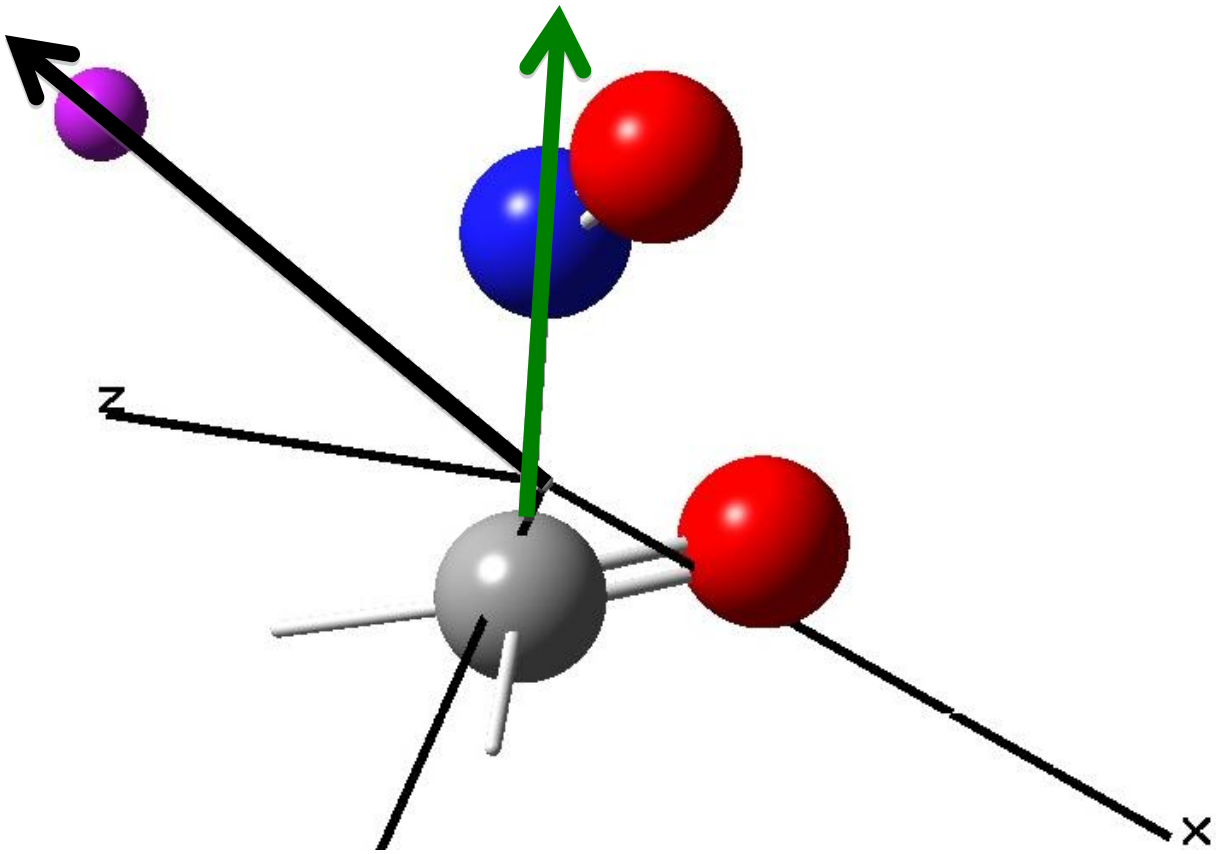

Figure S14: Ball and stick geometry of INT2 pre-dissociation, with the two methyl groups removed for clarity. The green vector lies on the C-N bond axis and represents the recoil vector experienced by the radical as it dissociates to NO + $CH_3C(O)CH_3$. The black vector represents the initial C-Br bond fission recoil vector and has been mapped onto the INT2 geometry. The Cartesian axes have their origin at the center of mass for this geometry. This center of mass is preserved from the precursor $CH_3C(NO_2)(Br)CH_3$ upon mapping and as such the initial C-Br recoil vector (black) remains at the center of mass (origin of axes). The angle between the black and green vectors is calculated to be ~68 degrees.

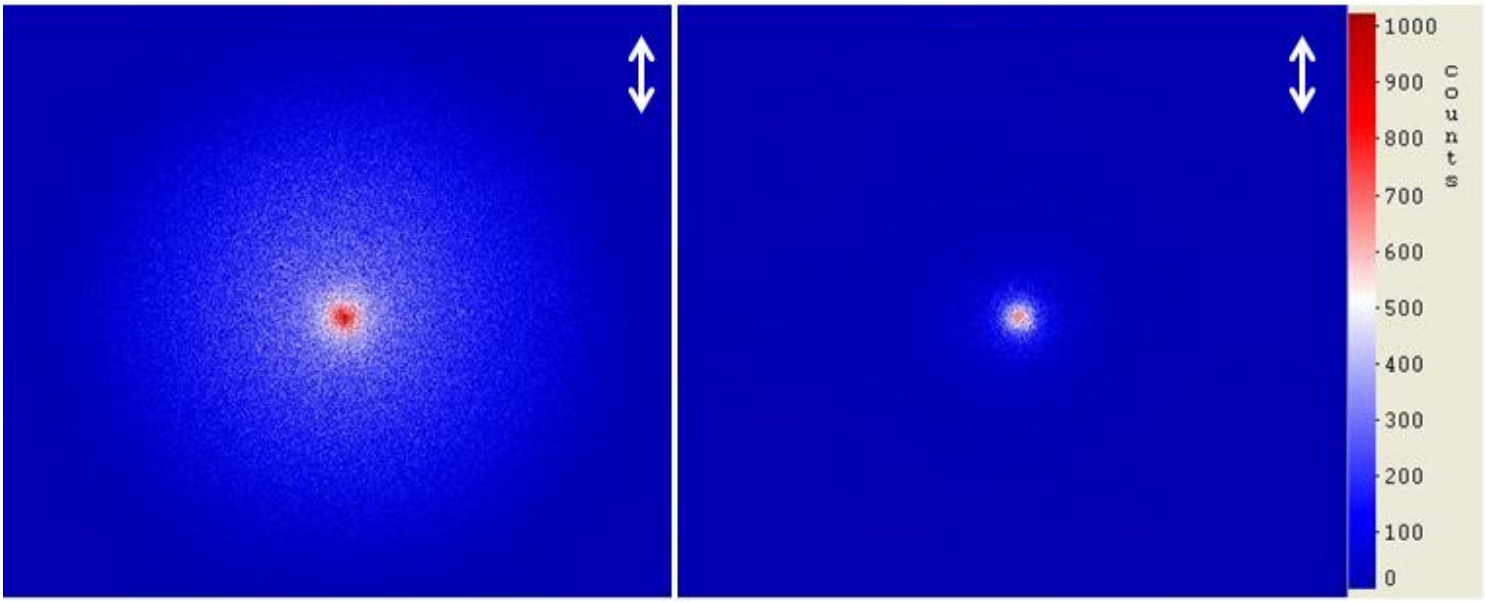

Figure S15: Ion images at m/e=43 (CH_3CO^+) taken on the velocity map imaging apparatus. The left frame shows the total (Signal + Background) image and the right frame shows the background image. Both images measure 786 x 698 pixels (W x H). In both images the white arrow shows the polarization of the photolytic laser.

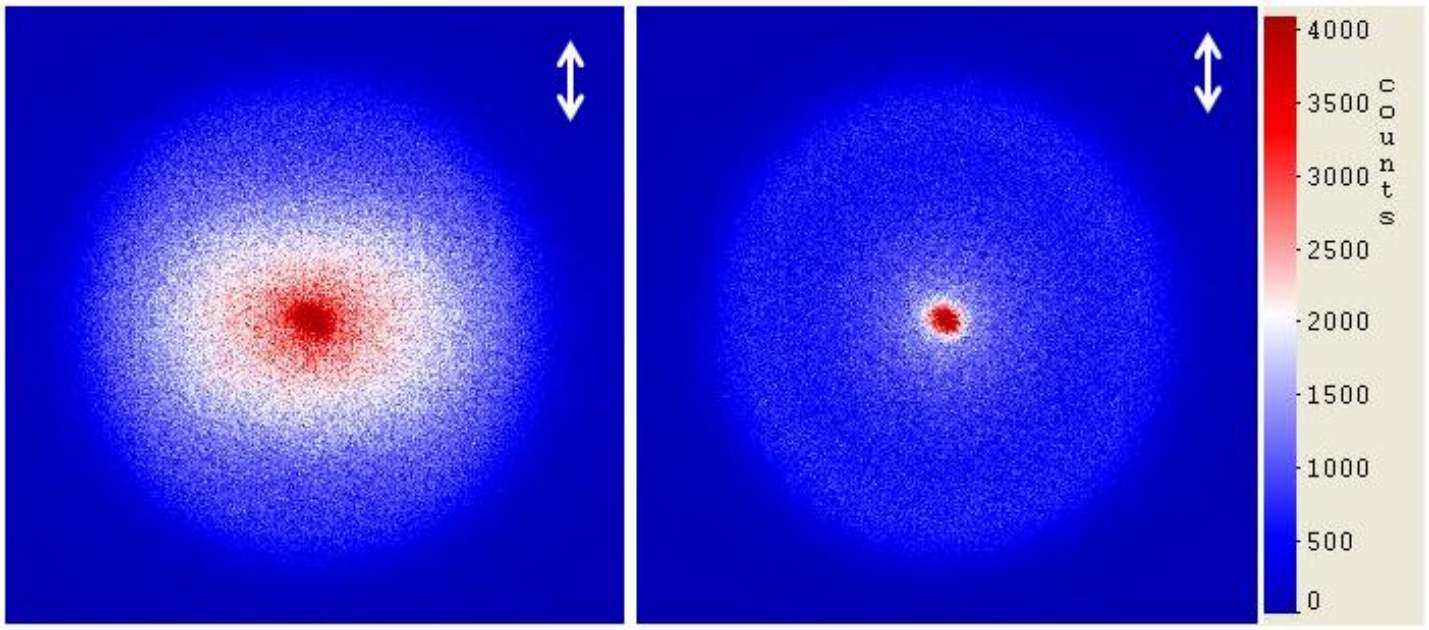

Figure S16: Ion images at m/e=123 ($CH_3C(Br)CH_3^+$) taken on the velocity map imaging apparatus. The left frame shows the total (Signal + Background) image and the right frame shows the background image. Both images measure 304 x 302 pixels (W x H). In both images the white arrow shows the polarization of the photolytic laser.

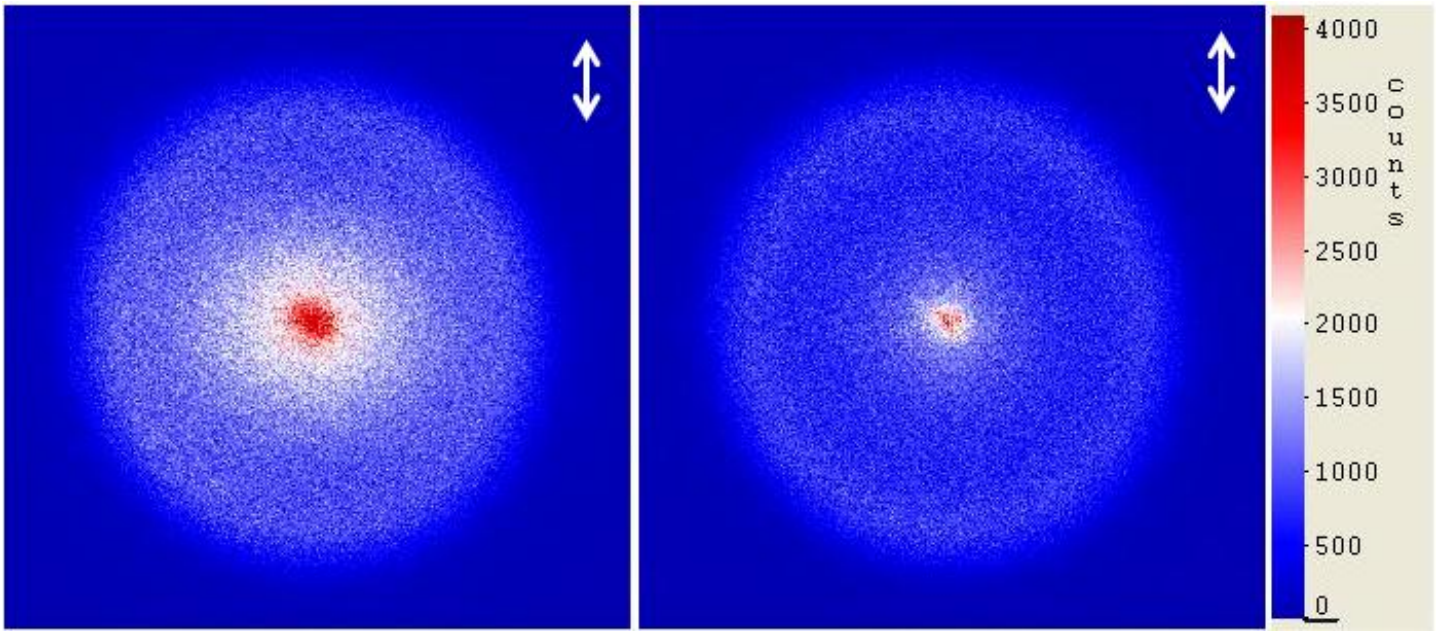

Figure S17: Ion images at m/e=122 ($CH_2C(Br)CH_3^+$) taken on the velocity map imaging apparatus. The left frame shows the total (Signal + Background) image and the right frame shows the background image. Both images measure 304 x 302 pixels (W x H). In both images the white arrow shows the polarization of the photolytic laser.

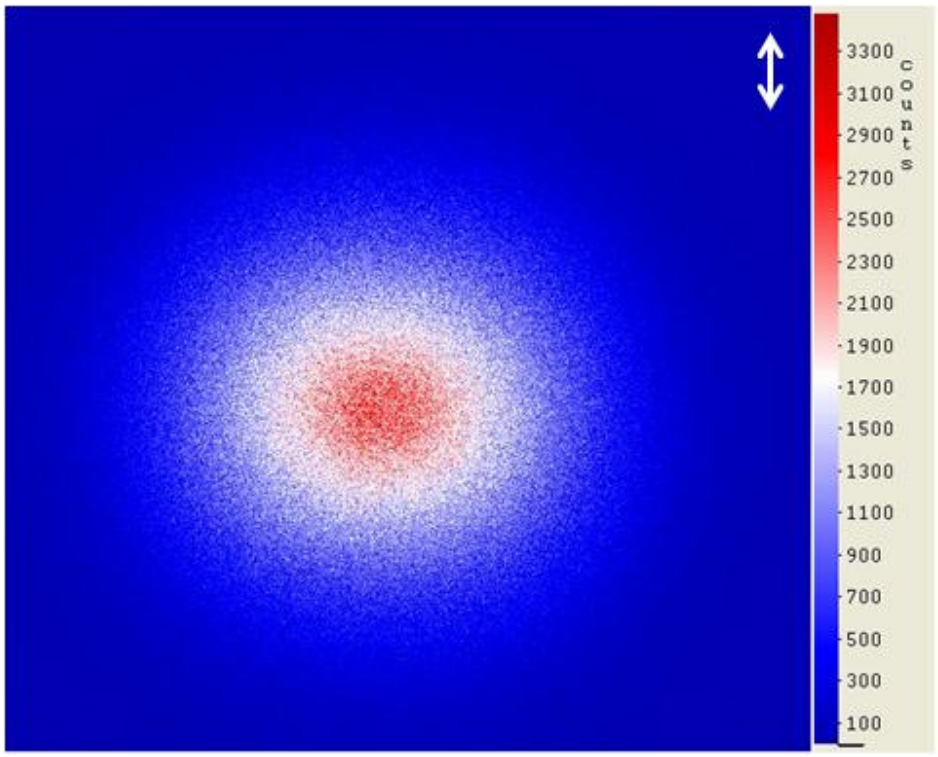

Figure S18: Ion image at m/e=41 ($CH_3CCH_2^+$) taken on the velocity map imaging apparatus. This image represents the total signal at m/e=41. The background was less than 3% of the total signal and thus is not shown. The image measures 525 x 487 pixels (W x H). In both images the white arrow shows the polarization of the photolytic laser.

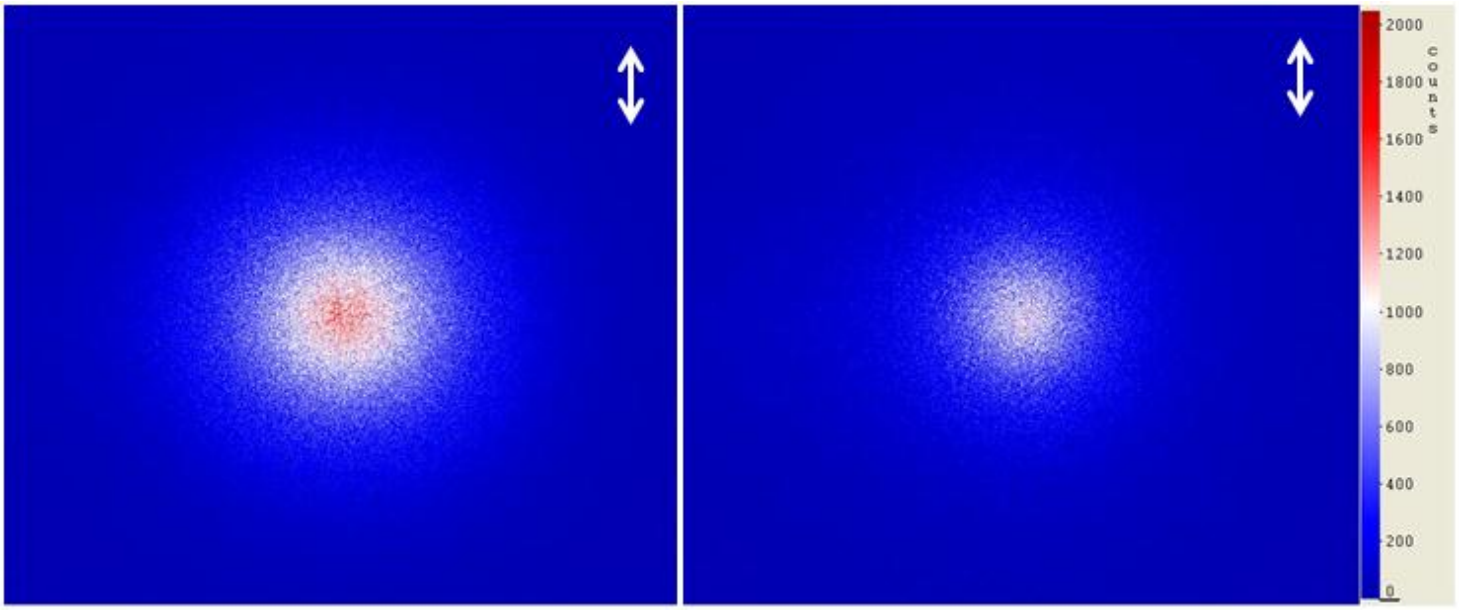

Figure S19: Ion images at m/e=41 ($CH_3CCH_2^+$) taken on the velocity map imaging apparatus at 8.87 eV ionization energy. The left frame shows the total (Signal + Background) image and the right frame shows the background image. Both images measure 566 x 502 pixels (W x H). In both images the white arrow shows the polarization of the photolytic laser.

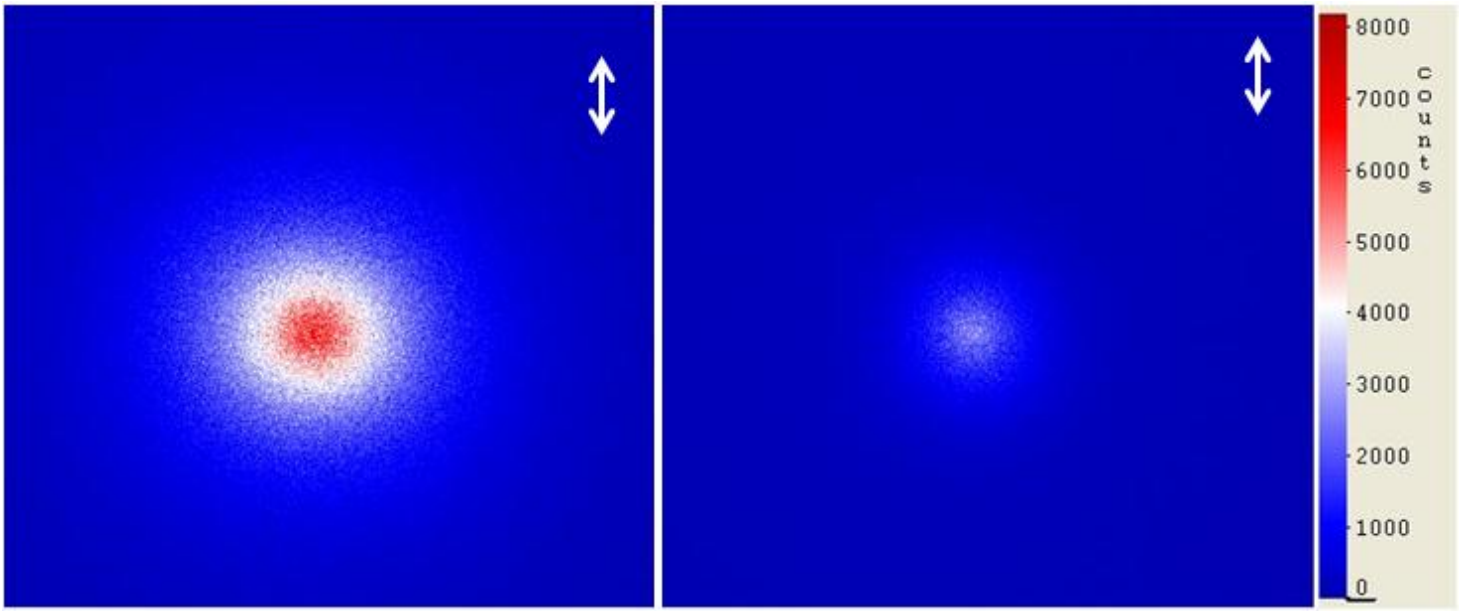

Figure S20: Ion images at m/e=42 ($C_3H_6^+$/CH_2CO^+) taken on the velocity map imaging apparatus. The left frame shows the total (Signal + Background) image and the right frame shows the background image. Both images measure 372 x 343 pixels (W x H). In both images the white arrow shows the polarization of the photolytic laser.

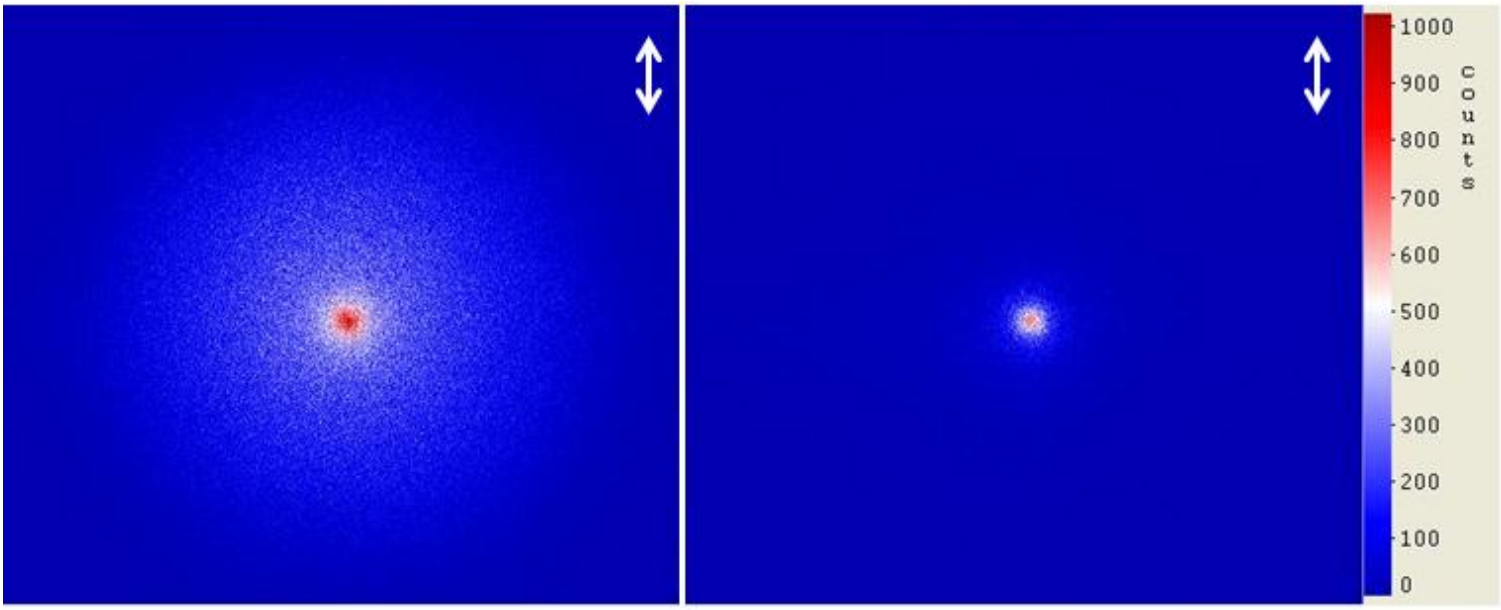

Figure S21: Ion images at m/e=43 (CH_3CO^+) taken on the velocity map imaging apparatus. The left frame shows the total (Signal + Background) image and the right frame shows the background image. Both images measure 786 x 698 pixels (W x H). In both images the white arrow shows the polarization of the photolytic laser.

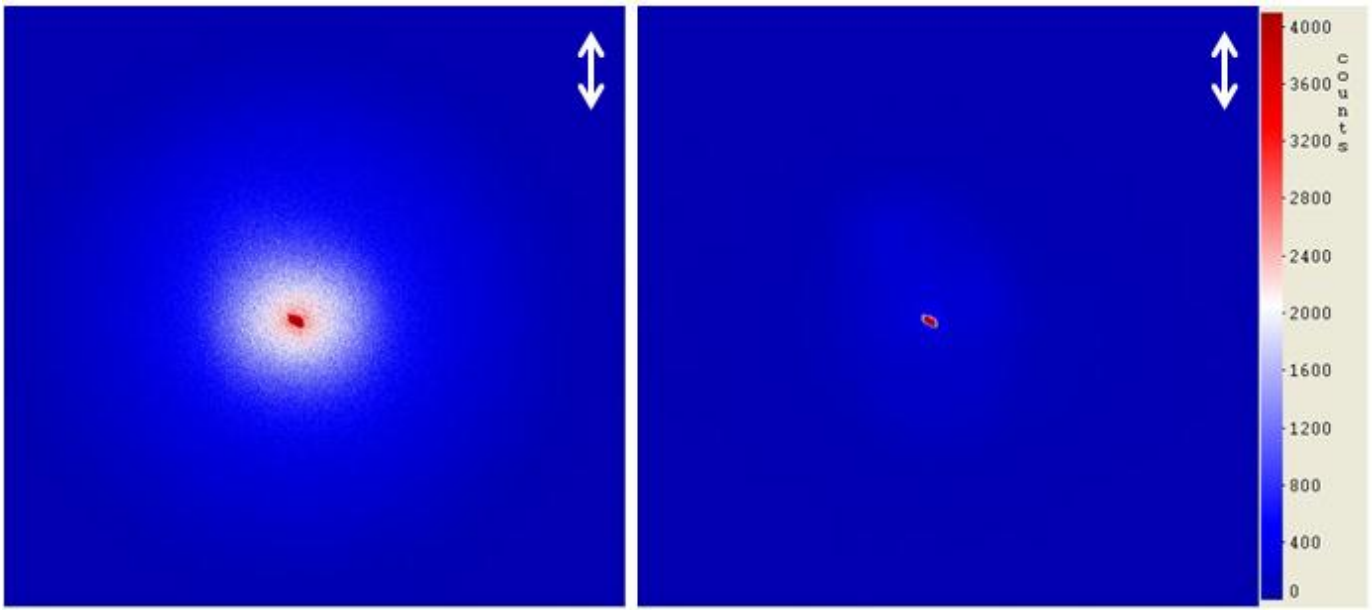

Figure S22: Ion images at m/e=30 (NO^+) taken on the velocity map imaging apparatus. The left frame shows the total (Signal + Background) image and the right frame shows the background image. Both images measure 916 x 886 pixels (W x H). In both images the white arrow shows the polarization of the photolytic laser.